IOP Publishing Nanotechnology
Nanotechnology **22** (2011) 445601 (11pp) doi:10.1088/0957-4484/22/44/445601

Linker-mediated assembly of gold nanoparticles into multimeric motifs

Mateusz Sikora[1], **Piotr Szymczak**[2], **Damien Thompson**[3] **and**
Marek Cieplak[1]

[1] Institute of Physics, Polish Academy of Sciences, Aleja Lotników 32/46, 02-668 Warsaw, Poland
[2] Institute of Theoretical Physics, Faculty of Physics, University of Warsaw, ulica Hoża 69, 00-681 Warsaw, Poland
[3] Tyndall National Institute, Lee Maltings, University College Cork, Cork, Ireland

E-mail: mc@ifpan.edu.pl

Received 14 May 2011, in final form 13 September 2011
Published 7 October 2011

Abstract
We present a theoretical description of linker-mediated self-assembly of gold nanoparticles (Au-NP). Using mesoscale simulations with a coarse-grained model for the Au NPs and dirhenium-based linker molecules, we investigate the conditions under which large clusters can grow and construct a phase diagram that identifies favorable growth conditions in terms of floating and bound linker concentrations. The findings can be considered as generic, as we expect other NP-linker systems to behave in a qualitatively similar way. In particular, we also discuss the case of antibody-functionalised Au NPs connected by the C-reactive proteins (CRPs). We extract some general rules for NP linking that may aid the production of size- and shape-specific NP clusters for technology applications.

(Some figures in this article are in colour only in the electronic version)

1. Introduction

Self-assembled synthetic nanostructures are expected to play a vital role in the construction of future devices, sensors, and materials. Metallic nanoparticles (NPs) are promising building blocks of such structures [1] because of their optical, conductive, plasmonic, and magnetic properties. The methods of their production were known to Faraday [2] and are well established [3]. They involve coating the NPs with surfactant molecules that stabilize their structure and prevent aggregation. Making extended structures then requires arranging the NPs into regular patterns, typically, through deposition on a substrate with NP coats interdigitated by weak non-covalent interactions. Examples of such an approach are given in [4–13].

Another way involves generation of chemical bonds between the NPs through intervening molecules or particles which go under the name of linkers. For instance, Pełka *et al* [14] and Liao *et al* [15] link gold NPs via conjugated dithiolated molecules. Here, we consider citrate-covered gold NPs [16, 17] linked by dirhenium-based molecules. These linkers have been synthesized by Lydon *et al* [18] and act as precursors to the formation of conducting molecular wires. They link gold NPs via their thiocyanate anchor groups to form molecular 'dumbbell' shapes [19]. A schematic view of the bonding provided by the dirhenium linkers is shown in figure 1.

In this paper, we construct a coarse grained description of the system containing citrate-protected gold NPs, dirhenium linkers, and implicit water and analyze the NP self-organisation into clusters. In this description, the NPs and linkers are represented by effective spheres. The sizes of the spheres reflect the sizes of the specific physical objects in the system. Nevertheless, our discussion can be considered as generic with the understanding that results may change quantitatively if NPs and linkers of different sizes are considered. We ask under what conditions large clusters can grow and construct a phase diagram that identifies favorable growth conditions. The phase diagram is set on the n_L–L/L_{max} plane, where n_L denotes the number density of the floating linkers in solution, L is the allowed number of linkers that can attach to an NP, and L_{max} is the maximum number of linkers that a bare, non-citrate coated NP could accommodate. L_{max} depends on the radius, R_{NP}, but it also depends on the way the linkers can pack the NP surface: it can either be random or be designed as a perfect tiling.

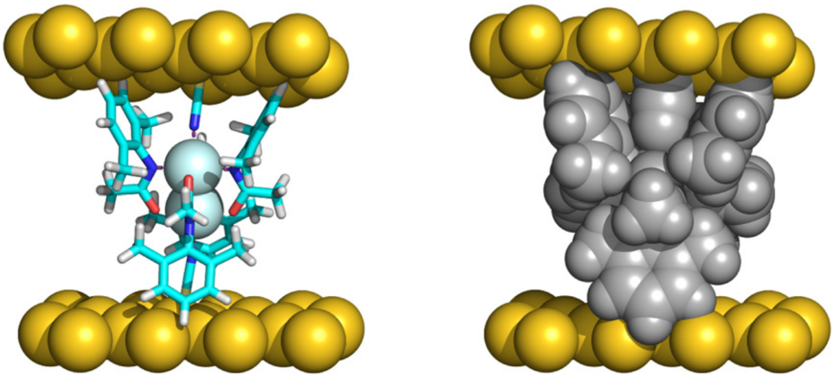

Figure 1. Atomic representation of the dirhenium linker binding two gold surfaces. In the left panel, two rhenium atoms are shown as the two central spheres. The thiocyanate anchor groups are shown as brighter tubes (one at the top, another at the bottom; in yellow online). The atoms of gold, at the top and the bottom, are shown as spheres. The remaining tubes in the decreasing sense of darkness (in red, green, and gray online) correspond to the oxygen, carbon, and hydrogen atoms. The top part of the linker is twisted by about 90° with respect to the bottom part and hence the appearance of no symmetry between the up and down directions. The sulphur–rhenium–sulphur angle is equal to about 11° [18]. The right panel shows the same system with each atom represented by its corresponding van der Waals sphere. This panel indicates that it is sensible to approximate the linker by a rigid, nearly spherical object.

In the random case, the calculation of $L_{\max}$ corresponds to the so-called random sequential adsorption process on the sphere [20] in which spheres of a given radius are randomly attached to the surface of a fixed sphere. Independent random spheres are added successively, provided there is no overlap with the previous spheres. We determine $L_{\max}$ through long simulations with one NP and many linkers. The simulation is stopped when there is a saturation in the number of linkers that can get attached. The results are shown in table 1 and these are the values of $L_{\max}$ that are used in this paper. The alternative perfect design would yield $L_{\max,\mathrm{p}} > L_{\max}$. The values of $L_{\max,\mathrm{p}}$ are also listed in table 1. They can be obtained from purely geometrical considerations as explained in the caption of table 1.

It should be noted that L differs from $L_{\max}$ because the thiocyanate-terminated linkers bind much more weakly than the carboxylate-terminated citrate coats [19]. The atomically non-uniform surface of gold results also in non-uniform binding energies of both linker and protector molecules [19], further complicating the process of linker/protector exchange. In principle, L has some dependence on the temperature, T, but it is mainly determined by the specifics in the morphology of the surfaces of the gold NPs (and thus by the manufacturing process). $L/L_{\max}$ is thus a measure of the effective fractional surface that can be mounted by linkers.

Table 1. Maximum number of linker molecules that can attach to a nanoparticle of given radius. The values of $L_{\max}$ were found through long Monte Carlo runs with one NP in a bath of linkers, with ϵ set according to the binding energetics calculated from [19] as described in the text. The values of $L_{\max,\mathrm{p}}$ corresponding to the perfect non-random placement can be derived by using the Hadwiger theory as cited in [21]. However, we use the following simple approach. Consider three spheres of radius R_{L} placed on the surface of a larger sphere of radius R_{NP}. We observe that when the three spheres touch each other then their points of contact with the large sphere set a spherical equilateral triangle. Its area is denoted by A_{t}. Twice the A_{t} gives the surface area covered by one sphere. The reason for the factor of two is that—in analogy to the planar hexagonal lattice—1/6 of the area covered by one sphere corresponds to 1/3 of the triangle spanned by three spheres (including the gap). Thus, knowing the total surface of the large sphere and A_{t} gives us $L_{\max,\mathrm{p}}$. We have [22] $A_{\mathrm{t}} = (3\theta - \pi)R_{\mathrm{NP}}^2$, where the triangular angle θ satisfies $\cos(\theta) = \frac{1}{2} - R_{\mathrm{L}}^2/(2R_{\mathrm{NP}}^2 + 4R_{\mathrm{NP}}R_{\mathrm{L}})$. In the limit of large R_{NP}, θ becomes 60°.

R_{NP} (nm)	$L_{\max}$	$L_{\max,\mathrm{p}}$	R_{NP} (nm)	$L_{\max}$	$L_{\max,\mathrm{p}}$
3	79	148	10	677	1129
5	186	313	13	1119	1860
6	255	435	15	1486	2449
7	346	579	17	1904	3118
8	453	742	20	2629	4273

We find that while the phase diagram depends on the NP radius it is only weakly sensitive to temperature, the scale of which is set by the depth of the linker-NP trapping potential. To model covalent junction formation correctly [15, 19], as opposed to just using non-covalent physical interweaving of the NPs [4–13], this potential morphs into a permanent bond upon arrival of the linker at the surface. In particular, we find that large clusters can grow at low floating linker densities n_{L} and in a broad region centered around a specific value, f, of surface coverage $L/L_{\max}$ and with a low cutoff, f_{c}, that defines the minimum linker fractional coverage below which NP linking terminates. We observe that the larger the R_{NP}, the smaller the f_{c}. Furthermore, the whole region of favorable growth moves toward smaller values of $L/L_{\max}$ while expanding upward, i.e. reaching increasing floating linker densities. For the typically used $R_{\mathrm{NP}} = 5$ nm, f_{c} is close to 0.2 which is above the experimentally accessible range of $L/L_{\max} \approx 0.05$ for the replacement of strong citrate protectors by weak dirhenium linkers on gold [19]. This low $L/L_{\max}$ provides discrete dimers [19] for plasmonic applications [23, 24]. Promoting formation of higher n-mer structures would require dealing with larger radii and/or allowing for higher linker surface coverages. Such coverages can be obtained by using weaker protecting coats and/or stronger-binding linker molecules, e.g. linkers with thiol instead of thiocyanate anchor groups.

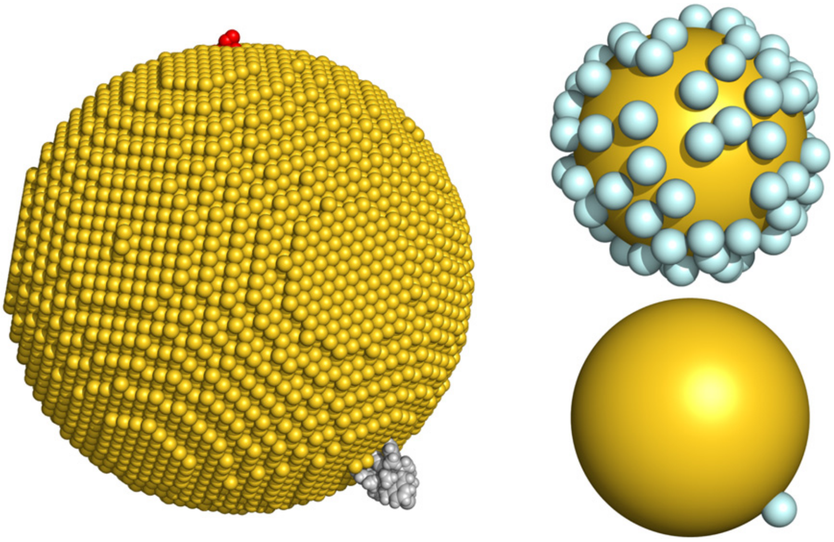

Figure 2. Construction of the gold NP model. The left panel shows an atomic representation of the NP. The gold atoms in the NP are drawn assuming the perfect fcc lattice. The radius of the NP is set to 5 nm. At the top of the NP, a single citrate protector molecule is shown (in red online). Such molecules cover most of the surface of the sphere. Only one of them is shown for clarity. At the bottom right of the NP, there is a protrusion representing a single dirhenium linker. In our coarse grained model, the linker and citrate-protected gold structures are represented by a small and large sphere as shown in the bottom right panel. The top right panel shows a single NP with many linkers attached to it.

Going beyond the dirhenium/citrate dumbbells [19], we move to the higher $L/L_{\max}$ region of the phase diagram in which conditions for larger cluster growth are met. This is done for a fixed number of the NPs. In general, the properties of clusters can depend on whether they are free in the bulk of the solution, deposited on a surface or embedded in a matrix of another material. In our simulations, we consider the free case because in the experimental situation [19] the clusters arrive fully formed on a substrate through a drying process.

Finally, we discuss the case of the system in which the gold NPs are connected by large C-reactive proteins (CRPs) instead of the rhenium linkers. Once both the proteins and the NPs are represented by spheres then a simple rescaling argument allows us to extrapolate some of the rhenium-derived results to the protein-NP system. We argue that this system is in a regime in which large clusters can arise.

2. Model and methods

2.1. The coarse grained model

Synthesis of gold nanocrystals through the citrate reduction of $AuCl_4$ results in nearly monodisperse icosahedral gold NPs (see, e.g. [25]). If one imagines cutting out a sphere of 5 nm radius in an fcc bulk gold lattice then one gets 20 000 as an estimate of the number of atoms that are enclosed. The surface atoms of the cut-out belong to various facets that intersect. Thus one can distinguish characteristic sites, including for example nine-coordinated flat terrace sites, six-coordinated ridge sites, and three-coordinated apex sites. While the surface of a true NP is certainly more complex and more disordered [26], these characteristic sites provide representative gold geometries for estimates of binding energies. Calculations presented in [19] lead to the conclusion that the dirhenium complex binds to terrace sites with an adsorption energy of between −0.2 and −0.1 eV, whereas the binding energies at the ridge and apex sites are −0.3 and −0.6 eV respectively. The citrate protecting coat, on the other hand, is much more strongly bound, with adsorption energies around 2–6 times that of the linker, with the relative likelihood of linker attachment highest at low coordination, e.g. apex, sites [19]. Hence $L/L_{\max}$ will be low, driving the system toward a large population of linked dimer structures.

The large number of atoms even in a small NP justifies taking a coarse grained theoretical approach in which a citrate-protected gold NP is represented by a sphere. Figure 1 shows the dirhenium linker in a binding arrangement between two gold surfaces. The distance between the two binding sulfurs is 1.2 nm and the transverse size is about 1 nm, so we may approximate it as a sphere of radius $R_L = 0.6$ nm. In our studies, the size of the linker particle is kept fixed while R_{NP} varies between 3 and 10 nm. The concepts of the coarse grained construction of our model are illustrated in figure 2.

When studying coated and charged NPs theoretically, one typically adopts the framework of the extended Derjaguin–Landau–Verwey–Overbeek model [27, 28], that takes into account van der Waals–London attraction, Coulomb repulsion, and steric repulsion at touching distances. In the system we consider, the attractive linker-NP interactions define the physics of the problem. In this context, the linker molecule can be considered as another NP, but one that is smaller than the gold NP. Thus the attraction of the linker to the gold NP can be described by the simple Lennard-Jones potential with a minimum set at the distance r of $R_{NP} + R_L$ and with the depth set equal to the binding energy, ϵ (see figure 3). If all linker attachment events were restricted to the apex sites, then a characteristic measure of ϵ would be 0.6 eV and the room temperature simulations would correspond to about $k_B T/\epsilon$ of

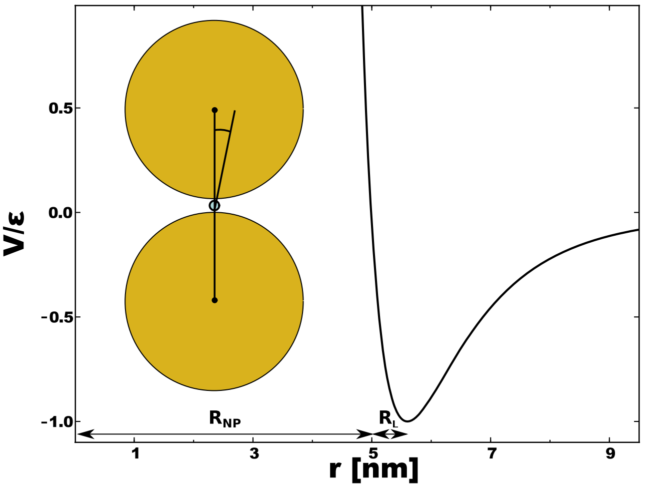

Figure 3. The main figure shows the NP-linker interaction potential for $R_{\mathrm{NP}} = 5$ nm. The radii of the interacting objects are indicated by the arrows. The inset on the left illustrates the angular condition on the attachment of one NP to another with one linker already adsorbed. The head-on interaction leads to attachment but so does a slightly skewed arrangement.

0.05, where k_{B} is the Boltzmann constant. The estimate of ϵ may, however, be lowered to allow for a broader selection of local environments on a curved surface to attach to, and to account for imperfections in the apex-like configurations. Thus it seems sensible to adopt $\epsilon = 0.25$ eV which corresponds to a room temperature of about $0.1\ \epsilon/k_{\mathrm{B}}$.

In order to simplify the model further, we assume that once a linker arrives at the gold NP it attaches to it permanently. At sufficiently high linker versus protector binding energy ratios the likelihood of linker/protector exchange increases and so a single NP can attach many linkers as shown in the top right panel of figure 2. The NP–NP and linker–linker interactions are of less importance and are accounted for merely by the steric constraints corresponding to soft repulsion as described by the Lennard-Jones potential which is truncated at minimum and shifted upward so that the interaction is purely repulsive.

The linker-mediated clustering of gold NPs is implemented in the following way. If an NP comes close to an NP with an already attached linker, it may bind at the unattached end of the linker. Linking is allowed only provided (a) the sulfur–sulfur axis within the linker forms an angle smaller than 11° with the surface normal direction of the arriving sphere (see figure 3) and (b) the distance between the center of the linker and the center of the sphere does not exceed $R_{\mathrm{NP}} + R_L + \delta R$, where δR is taken as $0.5 R_{\mathrm{L}}$, i.e. 0.6 nm. The reason for this particular angular constraint is the existence of a slight bend of 11° in the linker backbone [18].

Further attachment events may generate still bigger clusters of linked NPs. Each cluster is thought of as a rigid body with no internal degrees of freedom. It translates as a whole and rotates as a whole. A linker attached to an NP has an effect which is qualitatively similar to that of a patch placed on an NP to build in directionality. Such models have been discussed, for instance, in [29–34]. However, the goals of our model are different. It should be noted that the permanent character of the attachment events means that we study a non-equilibrium growth process instead of an equilibrium dynamics of linkers that can attach and then disengage (which would be a valid description for physically intertwined NPs, or indeed the present chemically linked system at high temperatures).

2.2. *The grand canonical Monte Carlo process*

We consider a fixed number of the NPs, N_{NP}, and variable number of the floating linkers. The mean number of free linkers is controlled by a chemical potential so that attachments of the linkers to the NPs do not deplete the population of the floating linkers, to model the experimental conditions of excess linker concentration [19]. In order to model this setup we employ the grand canonical Monte Carlo technique [35–38] in which, alongside the canonical Monte Carlo steps, the linker particles are inserted into the system or removed from it with a probability that depends on the chemical potential specified. The values of the chemical potential are selected in order to arrive at the required values of the linker density. In practice, most of the particle insertion events take place in regions of smaller instantaneous linker density. Since our focus is the non-equilibrium nature of the cluster growth process, we disallow linker detachment from NP as well as feeding the linkers back to the reservoir.

The canonical Monte Carlo steps involve attempting translational or rotational movements which are either accepted or abandoned according to the usual Metropolis Monte Carlo scheme [39]. The time scales of translational motion are set by diffusivity of the NPs and of the linkers. A single step in the linker movement involves crossing a random distance of between 0 and δr_{L} in a random direction. We have taken δr_{L} to be equal to 1 nm. This step is considered to be our adopted 'time' scale and 1 million of such steps is denoted as τ. Time, t, in this paper is measured in units of τ. The magnitude of a random displacement of an NP is reduced because linkers are much smaller in size. The Stokes–Einstein equation [40, 41], $D = k_{\mathrm{B}}T/6\pi\eta R$, where η denotes viscosity and D diffusivity, gives diffusivity of 40 $\mu\mathrm{m}^2\ \mathrm{s}^{-1}$ for a nanoparticle of $R_{\mathrm{NP}} = 5$ nm and about 20 times larger a number for the linker molecule. The maximum displacement of an NP in a single step is denoted by δr_{NP}. For R_{NP} of 10 nm we have selected δr_{NP} to be 0.1 nm. Values of δr_{NP} for other radii are obtained through scaling: they are equal to 0.12, 0.17, and 0.22 nm for R_{NP} of 8, 5, and 3 respectively.

Once a cluster is formed, its center of mass is translated with a reduced step size which is scaled down, compared to that of a single NP. The scaling depends on the effective radius, R, which is assumed to be proportional to $S^{1/3}$, where S denotes the number of the NPs in the three-dimensional cluster. We neglect the geometric effect of any attached linkers. In the overdamped Langevin dynamics, the mean square displacement is equal to $6Dt$. Thus the Monte Carlo step size, δx, should be proportional to $D^{1/2}$. Since $D \sim 1/R$, δx should scale as $R^{-1/2}$ and thus as $S^{-2/3}$. In addition to the translation, the cluster is allowed to rotate around its center of mass. We pick the rotation axis randomly and rotate the cluster by $\Delta\theta$. The rotational diffusion coefficient, D_{R}, is given by $D_R = \frac{k_B T}{8\pi\eta R^3}$ [42], i.e. it scales by the inverse of the volume, i.e. as S^{-1}. Thus the angular step size of rotations $\Delta\theta$ is reduced in proportion to $S^{-1/2}$ from the starting single sphere value of $\delta\theta_1$. It should be noted that once an NP acquires linkers, its rotation generates a new configuration. Most of our calculations are at $k_B T = 0.1\epsilon$ for which we take $\delta r_L = 1$ nm and $\delta\theta_1 = 15°$. Simulations at other temperature require scaling these parameters in proportion to T.

We have imposed periodic boundary conditions with the size of the simulation box varying between 100 and 200 nm depending on the size and number of the NPs. The number density of the NPs was kept at 5×10^{-6} nm^{-3}. For R_{NP} not exceeding 5 nm, we typically considered N_{NP} equal to 50. For R_{NP} equal to 8 nm and 10 nm, N_{NP} was set to 169 and 400 respectively. The instantaneous linker density, $n_L(t)$, reaches a stationary state corresponding to a set value of the chemical potential and fluctuates around n_L in this state. It is this equilibrated value that is used to characterize the growth conditions. In the transient period, $n_L(t)$ keeps adjusting to the available volume (some of which is excluded by the cores of the NPs).

2.3. Attachment of linkers to nanoparticles

Geometrical considerations suggest that the maximum theoretical coverage of a single NP by the linkers, $L_{\max}$, should grow as the second power of the radius. The values of $L_{\max}$ for the dirhenium linkers and several choices of R_{NP} are listed in table 1. As explained in the introduction, for weak linkers replacing strong protector adsorbates, the technique used experimentally to generate plasmonic gold dimers [19], only a small fraction of the NP surface area is available for the actual attachment. Nevertheless, it is instructive in the context of self-organization of extensive, tightly bound multimeric NP mesostructures [43] to consider a broader choice of the values of the parameter $L/L_{\max}$.

The actual number of linkers, n_s, that get attached to a single NP approaches L in a process that is extended in time as illustrated in figure 4 for various sets of the parameters—in particular, for N_{NP} equal to 1 and 50. In the case of 50 NPs, the results on the coverage are averaged over all spheres (which makes the corresponding curves smoother than for a single sphere). The saturation process has been checked not to be described by a single exponential term. However, a characteristic time scale, τ_s, can still be defined, e.g. by taking the time needed to arrive at the occupation of $\frac{1}{2}L$. We observe that τ_s gets shorter as the temperature gets higher and it generally depends on all other conditions.

Some of the observations about τ_s are easy to understand: the larger the density of the floating linkers n_L, the faster the saturation; and the higher the temperature, the faster the process. It is interesting to note, however, that τ_s for 50 NPs is typically an order of magnitude longer than for a single NP provided all other conditions are kept the same. At first thought this observation seems striking as it suggests that the linkers do not 'invade' all spheres simultaneously which would indicate large screening and correlation effects. In fact, the effect has only to do with the way the simulational time is counted. Due to the nature of the non-equilibrium grand canonical process, one cannot define a number of Monte Carlo steps per particle. This is because the number of the particles is varying: the NPs coalesce into rigid clusters and the number of floating linkers is far from being fixed. In particular, one has to feed in and diffuse around of order LN_{NP} linkers to cover N_{NP} spheres. Thus the saturation of the spheres proceeds mostly in parallel, but many more linkers are involved compared to one sphere.

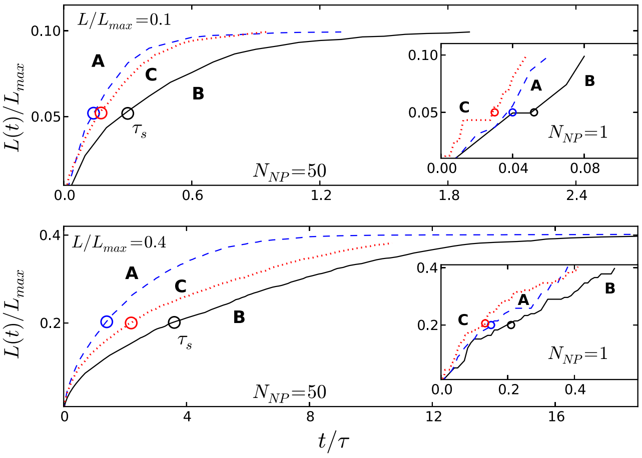

Figure 4. The fractional coverage, $L(t)/L_{\max}$, per NP as a function of time in single trajectories. The circles indicate the values of the half-times, τ_s. In each case, $R_{\mathrm{NP}} = 5$ nm and the values of $L/L_{\max}$ are indicated. In the main parts of the panels, $N_{\mathrm{NP}} = 50$. The insets are for $N_{\mathrm{NP}} = 1$. Conditions A correspond to $k_B T/\epsilon = 0.1$ and $n_L = 1.5 \times 10^{-4}$ nm^{-3}. Conditions B to $k_B T/\epsilon = 0.1$ and $n_L = 5 \times 10^{-5}$ nm^{-3}. Conditions C to $k_B T/\epsilon = 0.4$ and $n_L = 5 \times 10^{-5}$ nm^{-3}.

2.4. Formation of nanoparticle clusters

For a given density of the floating linkers and a fixed number of NPs we perform long numerical simulations with the goal of determining the aggregation pattern at a stage when all NPs are saturated at the allowed level specified by the value of L. In practice, this goal is difficult to achieve in the regime when larger clusters grow because of screening effects: a space next to a site available for adsorption of a linker may be hard to access because it lies in a 'cavity' formed by other NPs in the cluster or by other clusters. In such situations, we relax the conditions on terminating the simulation so that 90% (and sometimes 80%) of all possible adsorption sites are taken.

We find that the time intervals between successive linking events in NP aggregation may sometimes be broadly distributed. As a characteristic time scale, τ_a, for these events one may take a mean value of the distribution. Figure 5 shows examples of such distributions for two of the cases considered in the bottom panel of figure 4. A simple expectation is that an outcome of the NP aggregation process should be governed by the ratio of τ_a to τ_s. When this ratio is large, only small clusters will arise. When the two times are comparable, more linking will occur and so larger clusters will emerge. Even though the number of time steps in the simulations is only a rough measure of time, we indeed observe the connection between the type of growth and the relationship between τ_a and τ_s. For instance,

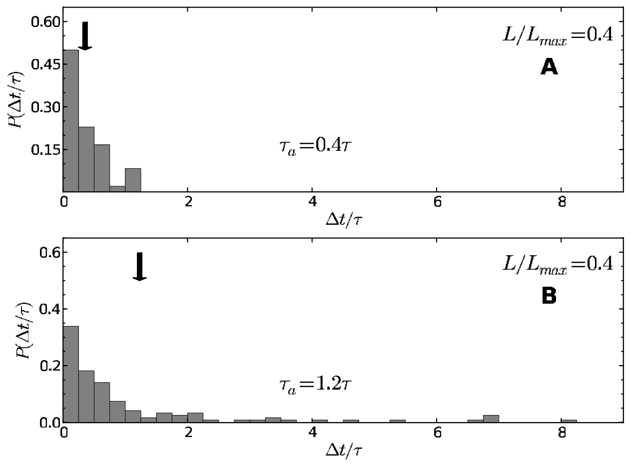

Figure 5. The distribution of 'time' intervals between successive events of NP aggregation. The arrows indicate values of the mean aggregation time. Both panels correspond to the bottom panel of figure 4. The top and bottom distributions correspond to conditions A and B.

for $L/L_{\max} = 0.4$ (see figures 4 and 5) we get $\tau_s = 1.4\tau$ and $\tau_a = 1.4\tau$ for conditions A under which only small clusters form. On the other hand, for conditions B, $\tau_s = 3.8\tau$ and $\tau_a = 1.2\tau$. In this case, only large clusters arise. It should be noted that any act of aggregation involves two NPs coming together but also making an appropriate alignment through a linker. We find that the diffusive encounter time of two NPs (calculated from the average separation between the particles and their relative diffusion constant) is much shorter than τ_a as it is of order 0.006τ for both conditions.

3. Results

3.1. Phase diagrams for growth

We observe that the aggregation process may lead either to the formation of many small clusters or to a distribution, $P(S)$, which gradually decreases with cluster size S which indicates that large clusters appear as well. The conditions that favor the growth of small clusters should correspond to an exponentially decaying distribution with a small related characteristic scale, ξ, the correlation length. In contrast, we expect on general grounds that the larger cluster growth regime corresponds to a distribution that decays with S as a power law (see, e.g. [44, 45, 48]) suggesting that the aggregation process is effectively scale free. The difference between the two behaviors is illustrated in figure 6 which shows examples of the distribution of cluster sizes and the corresponding plots of $\Pi(S)$. Here, $\Pi(S)$ denotes the number of clusters with sizes that are bigger than S (this quantity is typically less influenced by the noise in the data than the distribution itself). In the exponential regime, we have

$$\Pi(S) \sim \exp(-S/\xi) \tag{1}$$

and in the power law regime

$$\Pi(S) \sim S^{\alpha}. \tag{2}$$

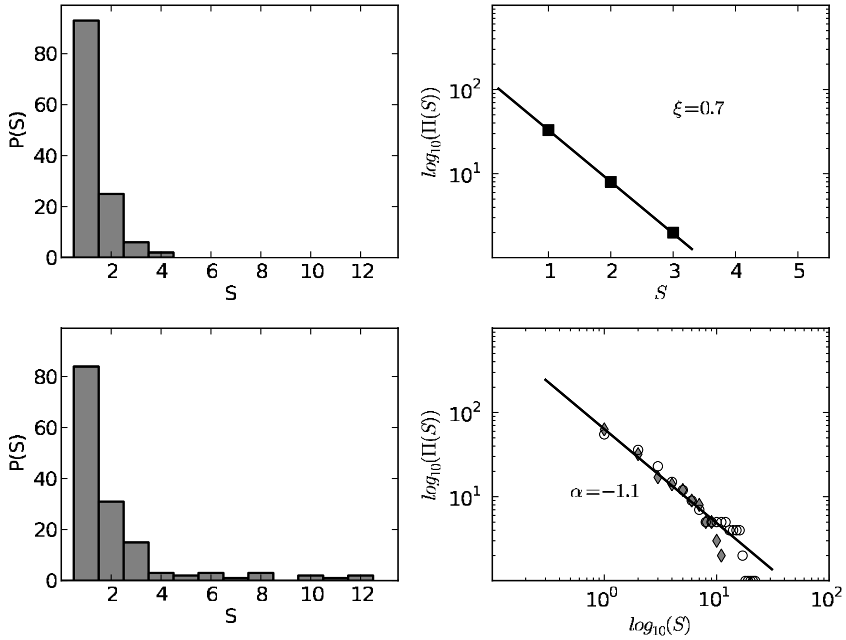

Figure 6. The top two panels illustrate growth in the regime which leads to clusters of small sizes whereas the bottom panels show the regime in which large clusters arise. The parameters corresponding to the lower panel are: $R_{\rm NP} = 5$ nm, $L/L_{\max} = 0.45$, $n_{\rm L} = 4 \times 10^{-5}$ nm^{-3}. The parameters corresponding to the upper panel are: $R_{\rm NP} = 10$ nm, $L/L_{\max} = 0.4$, $n_{\rm L} = 5.5 \times 10^{-5}$ nm^{-3}. The left panels show the distribution of clusters at 5% of final time when all NPs are saturated by linkers. The upper right panel shows a fit of $\Pi(S)$ to the exponential law, using the data in the upper left panel. The value of the correlation length ξ is indicated. In this case, the distribution $P(S)$ is non-zero for S of 1, 2, 3, and 4 which leads to three non-zero values of $\Pi(S)$ (for 1, 2, and 3). The lower right panel shows a fit to the power law. The solid diamonds correspond to 5% and the open circles to 25% of the final time. The value of the power law exponent is indicated.

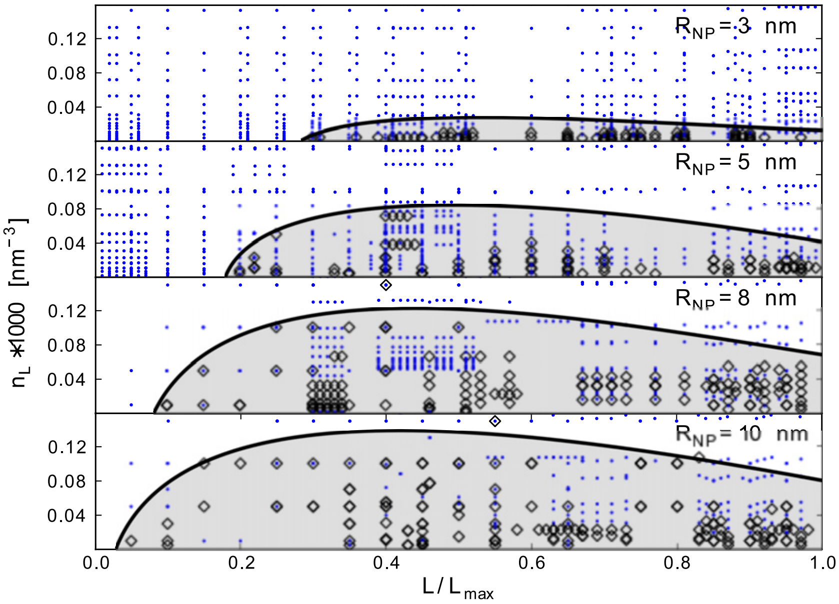

Figure 7. The phase diagram for the linker-mediated growth for the indicated values of R_{NP}. The contours delineate approximate boundaries of the scale free aggregation. The diamonds indicate a detected power law distribution of cluster sizes whereas the dots indicate evidence for the presence of only small clusters. The top panel also corresponds to the system of gold NPs linked by C-reactive proteins (discussed in section 3). The NPs are covered by antibodies. The case in which all of the antibodies are functional corresponds to $L/L_{\max} = 0.78$. If six of the antibodies are functional (the lowest observed value) then $L/L_{\max}$ is 0.08.

The data points in the top panels of figure 6 correspond to ξ of 0.7 while those in the bottom panels to $\alpha = -1.1$. Within the error bars, the power law exponent is consistent with the value of -1 (which corresponds to the distribution $P(S)$ decaying with S with the exponent of -2) obtained by Meakin [48] for the diffusion-limited cluster–cluster aggregation. We observe that whenever the power law appears to be valid in our simulations, the corresponding exponent is approximately universal.

The task at hand is to map out the boundary between the two regimes on the $n_{\mathrm{L}} - L/L_{\max}$ plane. The difficulty involved is that due to the intrinsically many body character of the potential generated by a cluster and the resulting heavy computational costs, our simulations are restricted to small numbers of NPs and small system volumes. These restrictions perturb the nature of the growth at its later stages through excessive influence of one growing cluster on another and overall final 'gelation'. It is thus sensible to assess the nature of the growth at its early stages, i.e. in the so-called flocculation regime [46–48], to borrow a term from colloid science. Another reason to study the early stages is that the growth parameters are not sensitive to the choice of the number of NPs that are used in the simulations (we adjust N_{NP} and keep the number density fixed, within the limits of the numerical feasibility). In figure 6 the early stage is defined operationally as corresponding to 5% of the final time—the time at which each NP has its maximum linker coverage. An extension to 25% still seems to be in the early stage as the shift away from the power law behavior only becomes apparent at larger values of S (the bottom right panel).

It is useful to think of the two functional growth laws as two faces of one law [48]:

$$\Pi(S) \sim S^{-\alpha} f(S/S^*), \qquad (3)$$

where S^* is a characteristic mean cluster size. The scaling function $f(S/S^*)$ is nearly constant for $S < S^*$ and rapidly falling for $S > S^*$. The exponentially decaying $\Pi(s)$ or $P(S)$ thus corresponds to small values of S^*. On the other hand, the power law is observed when S^* is large. In practice, our procedure is as follows. If the sizes of all clusters do not exceed two NPs, the situation is associated with the growth of small clusters only (this is the regime in which the plasmonic gold NP dimers [19] form). If there are clusters with $S \geqslant 3$, we fit the first three values of $\Pi(S)$ to the exponential function and determine the corresponding ξ. If ξ is below a threshold, the corresponding growth is identified as limited exponentially. Otherwise, we infer that the power law actually applies. The threshold of 1.5 has been selected as an apparent characteristic value separating the two growth behaviors. This approximate procedure leads to the results shown in figure 7 which delineates the boundary between the two types of early stage growth for four values of R_{NP} at $k_{\mathrm{B}}T = 0.1\epsilon$. It should be noted that there are substantial error bars in the precise location of the boundaries due to the limited statistics, deficiencies in the concept of the Monte Carlo time, and determination of the true 'stationary' value of the linker density that the growth process should be associated with. Also, the finite size of the system leads to fluctuations that blur the boundary.

Figure 7 suggests that the favorable conditions for growth of the large clusters (as indicated by the shaded areas) occur when n_{L} is small and $L/L_{\max}$ exceeds the cutoff value f_{c} which grows with increasing R_{NP}. The values of f_{c} correspond to about 0.3, 0.2, 0.1, and 0.05 for R_{NP} = equal to 3, 5, 8, and 10 nm respectively. The shaded region also keeps rising toward the higher values of n_{L} as R_{NP} increases and then decreases after reaching a maximum. The latter effect is connected with the fact that as $L/L_{\max} \to 1$ it becomes increasingly harder

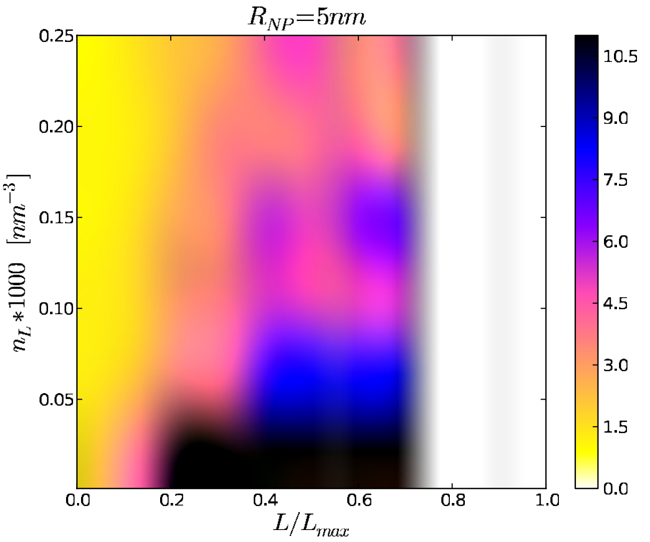

Figure 8. The sizes of largest clusters obtained for maximal linker coverage at the end of the evolution. The sizes are shown on the $n_\mathrm{L} - L/L_\mathrm{max}$ plane for $R_\mathrm{NP} = 5$ nm and $k_\mathrm{B}T = 0.1\epsilon$. The region with the largest clusters is shown in black and with the smallest in yellow. The color allocation has been determined by making a grid on the plane and by taking a mean over the data points within the grid. The grid size is 0.1 along the L/L_max axis and 0.05 × 1000 along the other axis. The scale of the color allocation is shown on the right. The white regions indicate a lack of any data points.

for the linker attached to a NP to find an empty spot on another NP to attach to. Finally, we note that the range of favorable conditions for the cluster growth increases with the NP radius, which reflects the increasing number of possible attachment spots with R_NP.

We now focus on the final stage of the aggregation. Figure 8 shows the field of sizes of the largest clusters on the $n_\mathrm{L} - L/L_\mathrm{max}$ plane for $R_\mathrm{NP} = 5$ nm. The field has been obtained by averaging the maximal values of S over pixels defined on a grid. The color coding combines all average sizes that are larger than 11 into one color. We observe that the largest clusters coincide with the shaded region identified in figure 7 by considering the early stages of growth. The final outcome of the evolution is thus consistent with the nature of growth at the early stages.

It should be noted that a substantial rise in the temperature limits the growth of large clusters. This point is illustrated in figure 9. Thus the T-dependence of the aggregation process, under the typical conditions given in figure 9 of small NPs with significant linker coverages and excess floating linker concentrations, is more influenced by the effective linker adsorption energy ϵ than by the linker diffusion coefficient.

3.2. Geometry of large clusters

Controlling the degree of aggregation of covalently linked NPs into clusters is central to current [15, 19] and emerging applications of mesostructures self-organized from nanostructured building blocks. For example, generation of sheet-like clusters would facilitate reaching applicational goals of the linker-connected networks of gold NPs in electronic devices [49] while reproducible 3D shapes could be integrated into next-generation 'beyond CMOS' 3D architectures [50]. In our simulations, some of the grown large clusters do have a sheet-like appearance but other shapes appear as well. In order to characterize the shape of a cluster we determine its center of mass tensor of inertia, determine its three eigenvalues, I_λ (with $\lambda = 1, 2, 3$), and the corresponding effective radii, R_λ. The radii are defined as $\sqrt{I_\lambda/S}$. In this definition, each NP contributes a unit mass and the linkers do not count. The R_λs are a generalization of the concept of the radius of gyration into three components. We adopt the convention in which R_1 is the smallest, R_2 the intermediate, and R_3 the largest radius.

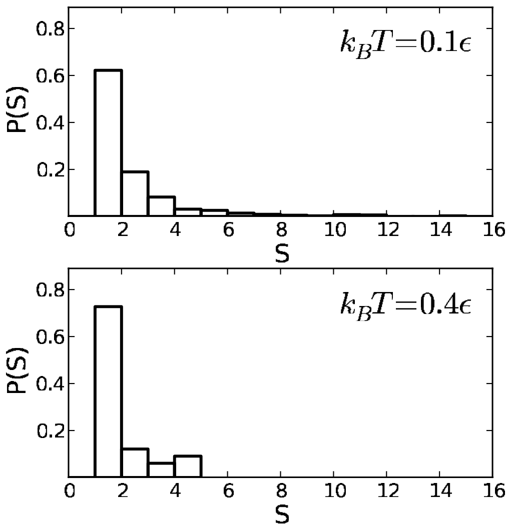

Figure 9. The temperature dependence of the cluster size distribution for the final stage clusters in the regime of the power law growth. The data points correspond to $R_\mathrm{NP} = 5$ nm, $L/L_\mathrm{max} = 0.4$, and $n_\mathrm{L} = 9 \times 10^{-5}$ nm^{-3}. The upper panel is for $k_\mathrm{B}T = 0.1\epsilon$ and the lower panel for $k_\mathrm{B}T = 0.4\epsilon$.

We combine the three radii into one parameter:

$$w = \frac{\Delta R}{\bar{R}} \tag{4}$$

where $\bar{R} = \frac{1}{2}(R_1 + R_3)$ and $\Delta R = R_2 - \bar{R}$. Clearly, when w is close to 0 the cluster is globular. Otherwise, one eigen-axis is distinct and an axial symmetry is dominant. Cigar-like objects correspond to R_2 being close to R_3 ($w \sim \frac{1}{2}(R_2 - R_1)$) and thus to substantial positive values of w. Planar objects correspond to R_2 being close to R_1 ($w \sim \frac{1}{2}(R_1 - R_3)$) and thus to substantial negative values of w. An additional characteristic of the cluster is provided by an average connectivity, C, which is defined as the average number of NPs that an NP is linked to. For an infinite square lattice, C (per particle) is equal to 2. C larger than 2 usually indicates the presence of three-dimensional connectivities, whereas smaller than 2 indicates the prevalence of chain-like connectivities.

Figure 10 shows examples of ten clusters together with their corresponding values of w and C. The clusters shown on the right-hand side of figure 10 are cigar-like. In contrast, the two clusters shown on the left-hand side are planar-like, but not strictly planar. Figure 11 shows the largest cluster that arose in

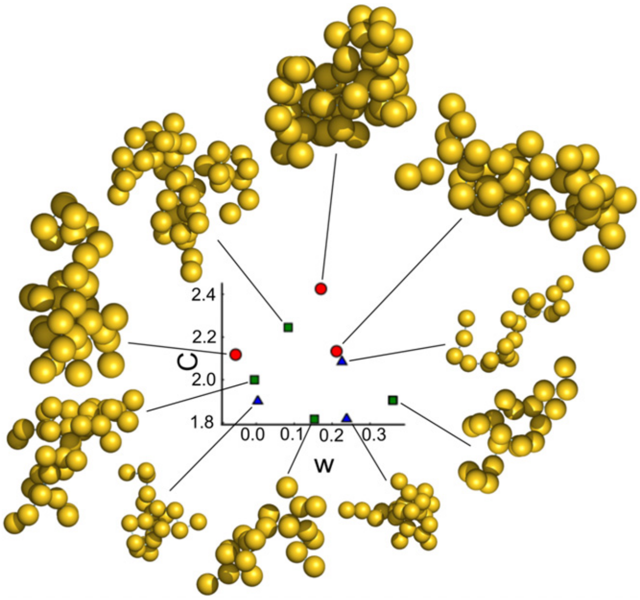

Figure 10. A sample choice of larger clusters with the associated values of the geometrical parameters w and C. For clarity, the only linkers that are shown are those which provide a connection between two NPs. The sizes of the spheres reflect the sizes of the NPs. The largest are for $R_{\mathrm{NP}} = 10$ nm, the smallest for 5 nm, and the intermediate for 8 nm.

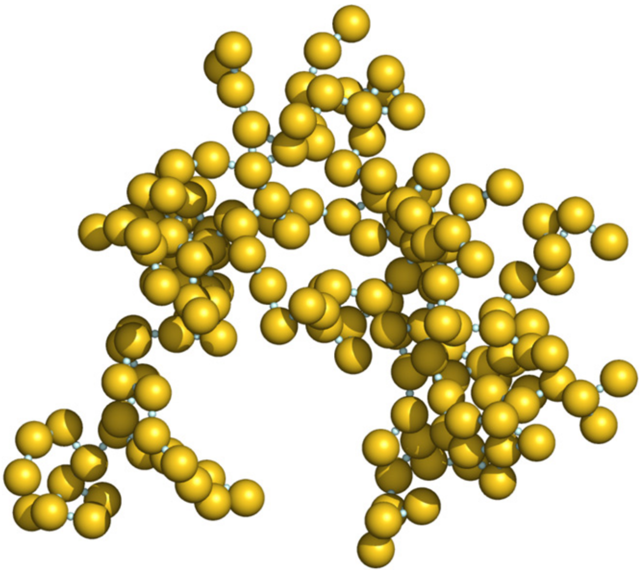

Figure 11. Example of a large cluster. It comprises 169 NPs and it has been generated for $R_{\mathrm{NP}} = 8$ nm, $k_{\mathrm{B}}T/\epsilon = 0.1$, $L/L_{\max} = 0.3$, and $n_{\mathrm{L}} = 8.09 \times 10^{-7}$ nm^{-3}. Its geometrical parameters are as follows: $C = 2.24$, $w = 0.042$, and the radius of gyration is 84.31 nm.

the simulations. It corresponds to $S = 169$, $w = 0.042$, and $C = 2.24$. This cluster has cavities, a large outside surface, and some chain-like linkages which leads to a C which may not immediately suggest a strong three-dimensional character. However, the cluster is fairly globular overall, as indicated by the small positive value of w.

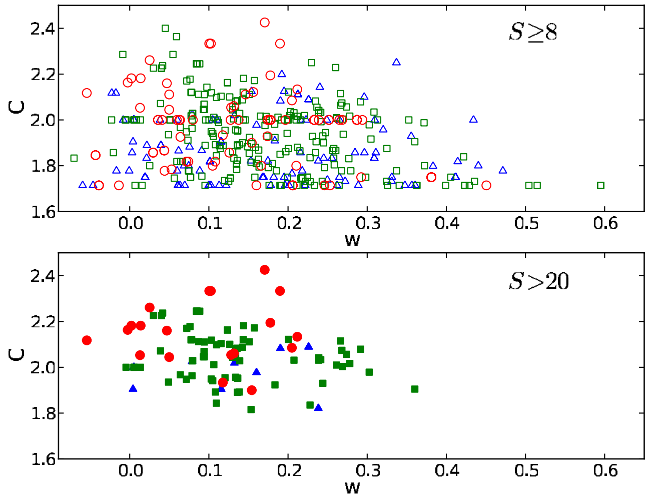

Figure 12. The w–C scatter plots for the clusters with $S \geqslant 8$. The triangles, squares, and circles correspond to R_{NP} of 5, 8, and 10 nm. The bottom panel shows just those clusters with $S > 20$.

Figure 12 shows the w–C scatter plot for clusters containing at least eight NPs. These geometrical parameters are not very meaningful if the clusters are too small and hence the cutoff of $S \geqslant 8$ was selected. Another selection adopted here is that we took only the largest clusters generated in each run. All values of $L/L_{\max}$ and densities considered are used to generate the plots in figure 12. The clusters with S larger than 8 (the top panel) have w between -0.09 and 0.6. The larger clusters tend to be more globular: w ranges between -0.08 and 0.36. We observe that conditions near the f_{c} (the low-L end of the shadowed regions in figure 7) seem to be favorable for a planar growth (negative w). Large positive values of w appear to require $L/L_{\max}$ of 0.4 or bigger, as would be expected from geometrical considerations of the 3D NP surfaces.

3.3. *C-reactive protein*

The C-reactive protein (CRP) is secreted in a human body [51] during the acute phase of the inflammation process. It activates the complement system that clears pathogens from the organism. CRP binds to molecules of phosphocholine that emerge on the surface of dead and dying cells such as those arising as a result of a heart attack. The CRP thus contributes to the buildup of scar tissue during the heart attack which diminishes the survival prognostics. The peak damage is caused during the first 5–50 h after heart failure. In this time window, monitoring the strength of the CRP response is vital for treatment. The raised CRP level in the blood plasma can also be used as a risk factor for future coronary heart disease or stroke [52, 53]. There is thus a need to develop a reliable and fast anti-CRP sensor chip.

One way to achieve this goal is to make use of the plasmonic properties of the colloidal gold. The surface plasmon resonance effect is enhanced when the NP–NP distance is reduced. The reduction is implemented by using small linkers of the kind discussed in the previous sections or those made of the larger CRP macromolecules. The structure of the CRP has been established through x-ray and AFM studies [53]. It is a pentameric molecule that is approximately toroidal in shape: the outer diameter is equal to 11.13 nm, the inner diameter to 3.52 nm, and the height to 3.03 nm. The active sites are placed on one of the top sides of the torus (i.e. a side—called the B-face—which is perpendicular to the five-fold symmetry axis).

In one of the proposed sensor systems [54], the gold NPs of $R_{\mathrm{NP}} = 20$ nm are covered by anti-CRP antibodies. These antibodies provide specificity to the CRP-based sensor system (a bare gold binds proteins in a non-specific way). It is not known where the antibodies bind to the CRP but the binding sites need not coincide with the active sites of the CRP. The exposed segments of the NP surface, i.e. those which do not get covered by the antibodies, are passivated by means of bovine serum albumin (BSA) to prevent non-specific binding. The thickness of the BSA layer is estimated to be between 2.3 and 7.2 nm [55] depending on the antibody concentration. The thickness of the layer made of the antibodies is about 6.2 nm [56]. Thus the effective R_{NP} of such covered NPs can be taken as 26.4 nm. Experimental results show that an effective number of antibodies adsorbed to each NP is about 62 [54]. However, not all of them stay functional. As few as six and as many as 62 are estimated to remain functional.

The CRP molecule is expected to bind to the functional antibodies and act like the rhenium linker, albeit of a larger size, connecting two NPs. In the simplest approach, we may model it as a sphere of $R_{\mathrm{L}} = 5.5$ nm which is half of the outer diameter. Thus for the gold-CRP system $R_{\mathrm{NP}}/R_{\mathrm{L}} \sim 4.8$ which is very close to the case of $R_{\mathrm{NP}} = 3$ nm considered for the gold–rhenium system. We expect then that the results obtained for R_{NP} in the previous sections, such as those shown in the top panel of figure 7, will apply to the gold-CRP system. However, there are several differences. One is that the experimental L/L_{max} will typically be larger than in the rhenium system. If all 62 antibodies are functional, then this number is close to the random dense packing limit of 79 for the effective radii of the spheres involved (see table 1). In this case, $L/L_{\mathrm{max}} = 0.78$ and the emergence of large clusters is likely. If few antibodies are functional, only small clusters will form. Generation of large clusters also requires adjustments in the NP concentration as too large a concentration may effectively 'clog' all active antibodies, preventing any further aggregation.

3.4. Summary

In summary, our results point to an important role of NP size in determining the size and shapes of the multimeric structures that may be assembled using covalent linker molecules. Fine-tuning of R_{NP} may provide further avenues to the routine production of functional n-mer motifs for technology applications. Improvements may also be obtained by further fine-tuning of the linker versus protector molecule adsorption energies to adjust the allowed coverage of a nanoparticle sphere by linkers, and perhaps also kinetic trapping of particular temporal structures using microfluidic chambers. Another feature to tinker with is to find ways to design non-random spots for the linker attachment, using, e.g. naturally occurring grain boundaries on the NP surface. Even though our discussion has been focused on gold NPs with rhenium linkers, its scope covers a more universal discussion of other systems needing adjustments in the sizes of the effective spheres. In particular, we have considered the gold NPs linked by proteins. We demonstrate that this system is more likely to form large clusters than the system with the rhenium linkers.

Acknowledgments

This work has been supported by the European Community's Seventh Framework Programme (FP7/2007-2-13) under agreement no. 213382 (FUNMOL) and through the Innovative Economy grant (POIG.01.01.02-00-008/08).

References

[1] Daniel M-C and Astruc D 2004 Gold nanoparticles: assembly, supramolecular chemistry, quantum-size-related properties, and applications toward biology, catalysis, and nanotechnology *Chem. Rev.* **104** 293–346
[2] Faraday M 1857 Experimental relations of gold (and other metals) to light *Phil. Trans.* **147** 145–81
[3] Turkevich J, Stevenson P C and Hillier J 1951 A study of the nucleation and growth processes in the synthesis of colloidal gold *J. Discuss. Faraday Soc.* **11** 55–75
[4] Motte L, Billoudet F and Pileni M P 1995 Self-assembled monolayer of nanosized particles differing by their sizes *J. Phys. Chem.* **99** 16425–9
[5] Harfenist S A, Wang Z L, Whetten R L, Vezmar I and Alvarez M M 1997 Three-dimensional hexagonal close-packed superlattice of passivated Ag nanocrystals *Adv. Mater.* **9** 817–22
[6] Korgel B A D and Fitzmaurice D 1998 Self-assembly of silver nanocrystals into two-dimensional nanowire arrays *Adv. Mater.* **10** 661–5
[7] Vossmeyer T, Chung S-W, Gelbart W M and Heath J R 1998 Surprising superstructures: rings *Adv. Mater.* **10** 351–3
[8] Sarathy K V, Raina G, Yadav R T, Kulkarni G U and Rao C N R 1997 Thiol-derivatized nanocrystalline arrays of gold, silver, and platinum *J. Phys. Chem.* B **101** 9876–80
[9] Hostetler M J, Stokes J J and Murray R W 1996 Infrared spectroscopy of three-dimensional self-assembled monolayers: N-alkanethiolate monolayers on gold cluster compounds *Langmuir* **12** 3604–12
[10] Fink J, Kiely C J, Bethell D and Schiffrin D J 1998 Self-organization of nanosized gold particles *Chem. Mater.* **10** 922–6
[11] Petit C, Taleb A and Pileni M P 1998 Self-organization of magnetic nanosized cobalt particles *Adv. Mater.* **10** 259–61
[12] Yin J S and Wang Z L 1997 Ordered self-assembling of tetrahedral oxide nanocrystals *Phys. Rev. Lett.* **79** 2570–3
[13] Kinge S, Crego-Calama M and Reinhoudt D N 2008 Self-assembling nanoparticles at surfaces and interfaces *ChemPhysChem* **9** 20–42
[14] Pełka J B, Brust M, Gierłowski P, Paszkowicz W and Schell N 2006 Structure and conductivity of self-assembled films of gold nanoparticles *Appl. Phys. Lett.* **89** 063110
[15] Liao J, Mangold M, Grunder S, Mayor M, Schoenenberger C and Calame M 2008 Interlinking Au nanoparticles in 2D arrays via conjugated dithiolated molecules *New J. Phys.* **10** 065019
[16] Lin Y, Pan G-B, Su G-J, Fang X-H, Wan L-J and Bai C-L 2003 Study of citrate adsorbed on the Au(111) surface by scanning probe microscopy *Langmuir* **19** 10000–3

[17] Nichols R J, Burgess I, Young K L, Zamlynny V and Lipkowski J 2004 A quantitative evaluation of the adsorption of citrate on Au(111) using SNIFTIRs *J. Electroanal. Chem.* **563** 33–9

[18] Lydon D P, Spalding T R and Gallagher J F 2003 Substitution reactions of rhenium-chorlide bonds in [Re$_2$(DMAA)$_4$CL$_2$], (DMAA $=$ 2′,6′-dimethylacetanilido); synthesis and characterisation of [Re$_2$(DMAA)$_4$X$_2$] (X $=$ NCO, NCS, N3) and [Re$_2$(DMAA)$_4$L$_n$][SbF$_6$]$_2$ ($n = 2$, L $=$ pyridine; $n = 1L = 4,4'$-bipyridine) *Polyhedron* **22** 1281–7

[19] Quinn A 2011 private communication

[20] Rodgers R P C and Baddeley A J 1991 Nested Monte Carlo study of random packing on the sphere *J. Appl. Probab.* **28** 539–52

[21] Hansen-Goos H, Roth R, Mecke K and Dietrich S 2007 Solvation of proteins: linking thermodynamics to geometry *Phys. Rev. Lett.* **99** 128101

[22] Mungan C E 2011 www.usna.edu/Users/physics/mungan/Scholarship/SphericalTriangle.pdf

[23] Yang S-C, Kobori H, He C-L, Lin M-H, Chen H-Y, Li C, Kanehara M, Teranishi T and Gwo S 2010 Plasmon hybridization in individual gold nanocrystal dimers: direct observation of bright and dark modes *Nano Lett.* **10** 632–7

[24] Lal S, Link S and Halas N J 2007 Nano-optics sensing to waveguiding *Nature Photon.* **1** 641–8

[25] Kwon K, Lee K Y, Lee Y W, Kim M, Heo J, Ahn S J and Han S W 2007 Controlled synthesis of icosahedral gold nanoparticles and their surface-enhanced Raman scattering property *J. Phys. Chem.* C **111** 1161–5

[26] Jadzinsky P D, Calero G, Ackerson C J, Bushnell D A and Kornberg R D 2007 Structure of a thiol monolayer-protected gold nanopatricle at 1.1Å resolution *Science* **318** 430–3

[27] Derjaguin B and Landau L 1945 Theory of the stability of highly charged liophobic sols and adhesion of highly charged particles in solutions of electrolytes *Zh. Eksp. Teor. Fiz.* **15** 663–82

[28] Verwey E J W and Overbeek J Th G 1948 *Theory of the Stability of Lyophobic Colloids* (Amsterdam: Elsevier)

[29] Zhang Z and Glotzer S C 2004 Self-assembly of patchy particles *Nano Lett.* **4** 1407–13

[30] Zhang Z, Keys A S, Chen T and Glotzer S C 2005 Self-assembly of patchy particles into diamond structures through molecular mimicry *Langmuir* **21** 11547–51

[31] Bianchi E, Largo J, Tartaglia P, Zaccarelli E and Sciortino F 2006 Phase diagram of patchy colloids: towards empty liquids *Phys. Rev. Lett.* **97** 168301

[32] Singh C, Ghorai P K, Horsch M A, Jackson A M, Larson R G, Stellacci F and Glotzer S C 2007 Entropy-mediated patterning of surfactant-coated nanoparticles and surfaces *Phys. Rev. Lett.* **99** 226106

[33] Hermans T M, Broeren M A C, Gomopoulos N, van der Schoot P, van Genderen M H P, Sommerdijk N A J M, Fytas G and Meijer E W 2009 Self-assembly of soft nanoparticles with tunable patchiness *Nature Nanotechnol.* **4** 721–5

[34] Giacometti A, Lado F, Largo J, Pastore G and Sciortino F 2010 Effects of patch size and number within a simple model of patchy colloids *J. Chem. Phys.* **132** 174110

[35] Frenkel D and Smit B 2001 Understanding Molecular Simulation *From Algorithmsto Applications* (*Computational Science Series* vol 1) 2nd edn (San Diego, CA: Academic)

[36] Norman G E and Filinov V S 1969 Investigations of phase transitions by a Monte-Carlo method *High Temp.* **7** 216–22

[37] Oberholzer M R, Wagner N J and Lenhoff A M 1997 Grand canonical Brownian dynamics simulation of colloidal adsorption *J. Chem. Phys.* **107** 9157–67

[38] Wang S-M, Yu Y-X and Gao G-H 2006 Grand canonical Monte Carlo and non-equilibrium molecular dynamics simulationstudy on the seelctive adsorption and fluxes of oxygen/nitrogen gasmixtures through carbon membranes *J. Membr. Sci.* **271** 140–50

[39] Metropolis N, Rosenbluth A W, Rosenbluth M N, Teller A N and Teller E 1953 Equation of state calculations by fast computing machines *J. Chem. Phys.* **21** 1087–92

[40] Einstein A 1905 Ueber die von der molekularkinetischen Theorie der Waerme geforderte Bewegung von in ruhenden Fluessigkeiten suspendierten Teilchen *Ann. Phys.* **17** 549–60

[41] Dill K A and Bromberg S 2003 *Molecular Driving Forces* (New York: Garland Science) pp 327–8

[42] Debye P 1929 *Polar Molecules* (New York: Reinhold)

[43] Pileni M P 2005 *Nanocrystals Forming Mesoscopic Structures* (Weinheim: Wiley–VCH, John Wiley distributor)

[44] Barabasi A-L and Stanley H E 1995 *Fractal Concepts in Surface Growth* (Cambridge: Cambridge University Press)

[45] Kolb M, Botet R and Jullien R 1983 Scaling of kinetically growing clusters *Phys. Rev. Lett.* **51** 1123–6

[46] Vold M J 1963 Computer simulation of floc formation in a colloidal suspension *J. Colloid Sci.* **18** 684–95

[47] Goodarz-Nia I and Sutherland D N 1975 Floc simulation: effects of particle size and shape *Chem. Eng. Sci.* **30** 407–12

[48] Meakin P 1992 Aggregation kinetics *Phys. Scr.* **46** 295–331

[49] Peterle T, Ringler P and Mayor M 2009 Gold nanoparticles stabilized by acetylene-functionalized multidentate thioether ligands: building blocks for nanoparticle superstructures *Adv. Funct. Mater.* **19** 3497–506

[50] van Zeijla H W, Weia J, Shena C, Verhaara T M, Mauryb P and Sarroa P M 2010 From 2-dimensional lithography to 3-dimensional structures *ECS Trans.* **27** 421–6

[51] Macintyre S S, Kushner I and Samols D 1985 Secretion of C-reactive protein becomes more efficient during the course of the acute phase response *J. Biol. Chem.* **260** 4169–73

[52] Pepys M B *et al* 2006 Targeting C-reactive protein for the treatment of cardiovascular disease *Nature Lett.* **440** 1217–21

[53] Lin S, Lee C-K, Wang Y-M, Huang L-S, Lin Y-H, Lee S-Y, Sheu B-C and Hsu S-M 2006 Measurement of dimensions of pentagonal doughnut-shaped C-reactive protein using an atomic force microscope and a dual polarisation interferometric biosensor *Biosens. Bioelectron.* **22** 323–7

[54] Braven H 2011 private communication

[55] Zhou C *et al* 2004 Human immunoglobulin adsorption investigated by means of quartz crystal microbalance dissipation, atomic force microscopy, surface acoustic wave, and surface plasmon resonance techniques *Langmuir* **20** 5870–8

[56] Lu X Y, Huang Y and Ma C 2001 Evaluation of protein adsorption on chitosan surfaces with reflectometry interference spectroscopy *Sensors* **1** 148–60